Steger CR, Reijmer CH, Van Den Broeke MR, Wever N, Forster RR, Koenig LS, Kuipers Munneke P, Lehning M, Lhermitte S, Ligtenberg SR and others (2017b) Firn meltwater retention on the Greenland Ice Sheet: A model comparison. *Frontiers in Earth Science*, **5**, 3 (doi: 10.3389/feart.2017.00003)

Tada H, Paris PC and Irwin GR (1973) The stress analysis of cracks. *Handbook, Del Research Corporation*, **34**(1973)

Ultee L (2020) SERMeQ model produces a realistic upper bound on calving retreat for 155 greenland outlet glaciers. *Geophysical Research Letters*, **47**, 1–10 (doi: 10.1029/2020GL090213)

Ultee L, Meyer C and Minchew B (2020) Tensile strength of glacial ice deduced from observations of the 2015 eastern Skaftá cauldron collapse, Vatnajökull ice cap, Iceland. *Journal of Glaciology*, **66**(260), 1024–1033, ISSN 00221430 (doi: 10.1017/jog.2020.65)

van den Broeke MR, Kuipers Munneke P, Noël B, Reijmer C, Smeets P, van de Berg WJ and van Wessem JM (2023) Contrasting current and future surface melt rates on the ice sheets of Greenland and Antarctica: Lessons from in situ observations and climate models. *PLOS Climate*, **2**(5), 1–17 (doi: 10.1371/journal.pclm.0000203)

van der Veen CJ (1998) Fracture mechanics approach to penetration of bottom crevasses on glaciers. *Cold Regions Science and Technology*, **27**(3), 213–223, ISSN 0165232X (doi: 10.1016/S0165-232X(98)00006-8)

van der Veen CJ (2007) Fracture propagation as means of rapidly transferring surface meltwater to the base of glaciers. *Geophysical Research Letters*, **34**(1), 1–5, ISSN 00948276 (doi: 10.1029/2006GL028385)

van der Veen CJ and Whillans IM (1989) Force budget: I. Theory and numerical methods. *Journal of Glaciology*, **35**(119), 53–60

Vaughan DG (1993) Relating the occurrence of crevasses to surface strain rates. *Journal of Glaciology*, **39**(132), 255–266, ISSN 00221430 (doi: 10.1017/S0022143000015926)

Weertman J (1977) Penetration depth of closely spaced water-free crevasses. *Journal of Glaciology*, **18**(78), 37–46

Yang K and Smith LC (2016) Internally drained catchments dominate supraglacial hydrology of the southwest Greenland Ice Sheet. *Journal of Geophysical Research: Earth Surface*, **121**, 1891–1910 (doi: 10.1002/ 2016JF003927)

APPENDIX A – EXTENDED METHODOLOGY

On-ice GNSS station pairs

In 2023 we installed eight GNSS stations in a strain diamond configuration extending 4 km along flow from our field camp to the crevasse field draining the firn aquifer, and 1 km in the across-flow direction

(Fig. 1). Each station was equipped with a Trimble NetR9 receiver, recording at 15 second intervals, and a Zephyr Geodetic Antenna mounted to aluminum conduit installed within the snow and stabilized with snow anchors and guy lines. We process positions using the GNSS base station HEL2 (66.40116°N, -38.21570°E) mounted on bedrock near the terminus of Helheim Glacier, with a baseline length of 41 km. We determine kinematic site positions for on-site stations using carrier-phase differential processing relative to HEL2, implemented with TRACK software (Herring and others, 2010). Kinematic positions for each station were resolved at 30 second intervals to match the sampling rate of our base station HEL2. Station position timeseries has a formal error of $\sim$0.02 m in the horizontal direction.

We use the GNSS-station derived logarithmic strain rate, $\dot{\epsilon}$ (2) and Glen's Law to calculate the longitudinal stress as

$$\sigma = \sqrt[n]{\frac{\dot{\epsilon}}{A}} = \sqrt[3]{\frac{\dot{\epsilon}}{A}} \tag{A1}$$

where n is the flow law exponent taken to be $n = 3$, and A is the creep parameter. We use A for ice temperature $T = -10$°C where $A = 3.5 \times 10^{-25}$ Pa^{-3}s^{-1}.

Principal strain rates and surface stresses

We calculate primary principal strain rates using NASA MEaSUREs program Multi-year Greenland Ice Sheet Velocity Mosaic (Joughin and others, 2016) velocities. This velocity product comprises a year-round velocity average that is selected to be representative of the 1995–2015 period and has a pixel size of 250 m by 250 m. We smooth surface velocity, $\boldsymbol{v} = [u, v]$ (easting and northing), with a 1 km^2 Savitzky-Golay filter to derive two-dimensional horizontal, $[x, y]$, principal strain rates over Helheim Glacier (cf. Meyer and Minchew, 2018; Minchew and others, 2018; Poinar and Andrews, 2021). We calculate the more-extensional $\dot{\epsilon}_1$ and more-compressional $\dot{\epsilon}_3$ principal strain rates as,

$$\dot{\epsilon}_1 = \frac{1}{2}\left(\frac{\partial u}{\partial x} + \frac{\partial v}{\partial y}\right) + \frac{1}{2}\sqrt{\left(\frac{\partial u}{\partial x} - \frac{\partial v}{\partial y}\right)^2 + \left(\frac{\partial u}{\partial y} - \frac{\partial v}{\partial x}\right)^2} \tag{A2}$$

$$\dot{\epsilon}_3 = \frac{1}{2}\left(\frac{\partial u}{\partial x} + \frac{\partial v}{\partial y}\right) - \frac{1}{2}\sqrt{\left(\frac{\partial u}{\partial x} - \frac{\partial v}{\partial y}\right)^2 + \left(\frac{\partial u}{\partial y} - \frac{\partial v}{\partial x}\right)^2} \tag{A3}$$

to calculate principal stress σ_1 used as an input to our LEFM Model in (3).

Air temperatures

To approximate when the snow surface in our study area first reached the melting point in 2023, we use MERRA-2 climate reanalysis data (Rienecker and others, 2011). We start with the MERRA-2 daily aggregated statistics single-level diagnostics data (M2SDNXSLV; Global Modeling and Assimilation Office, 2015) for 2-meter air temperature on the MERRA-2 grid. These data are spaced by 0.5° latitude and 0.625° longitude, or ∼55 km by ∼42 km at our study area. To calculate air temperature at our field camp (surface elevation s=1,536 m), we regress MERRA-2 daily minimum, mean, and maximum temperatures against surface elevation at the five closest grid points to camp (Fig. 5). The centers of these grid boxes span surface elevations from 1,270 m to 2,015 m and are located 19 km (s=1,770 m) to 44 km (s=1,480 m) from our field camp.

Whaleback dune identification

Whaleback dune distribution (Fig. 7) was identified from satellite imagery acquired between 2015 and 2023. Information regarding imagery acquisition timing, sun elevation and azimuth is provided in (Table 1) to show dune presence in 2023 imagery is not caused by significant deviations in imagery acquisition timing when compared to earlier years.

Wind conditions

High wind speeds are required for dune formation making meteorological conditions important when considering dune formation processes and any potential interannual variability of dunes in our study area on Helheim Glacier. We compare dune orientation to wind direction data at the closest PROMICE weather station, `NSE`, located at 2,375 m a.s.l. 150 km west of our study area (Fausto and others, 2021; How and others, 2022). We use daily averaged weather station observations collected between 19 June 2021 through 8 February 2024. We resolve the wind direction during dune formation events by filtering the dataset to observations (n = 357) with wind speeds greater than 15 m s^{-1} as required for whaleback dune formation (Filhol and Sturm, 2015). Wind directions were within 129°–138° representing 21% of all high-wind observations (Fig. 6c).

To determine if the expansion of whaleback dunes to higher elevations observed in 2023 was caused by a change in wind conditions, rather than by a change in crevasse distribution, we compared wind speed measurements recorded by on ice weather stations from 1998 through 2023. We again use hourly data

Table 1. Whaleback dune extent mapping satellite imagery details

		offNadir angle	avg. sun azimuth	avg. sun elevation	vehicle
2023	2023-09-08T17:21:10	19.790424°	225.93018°	22.77251°	WV01
	2023-07-16T16:57:52	31.374704°	222.64685°	40.08236°	WV01
	2023-03-28T16:55:29	30.686329°	216.59718°	22.53433°	WV01
2022	2022-04-12T17:25:33	27.936016°	227.59021°	25.74466°	WV01
	2022-03-27T16:58:59	20.862982°	217.70584°	21.945127°	WV01
2021	2021-10-30T14:58:01	32.107082°	189.17178°	9.384423°	WV02
2020	2020-08-21T13:50:03	29.974792°	165.19173°	34.859047°	WV02
	2020-06-22T16:54:52	32.284256°	223.98341°	41.93131°	WV01
	2020-05-15T13:59:08	17.769472°	169.4692°	42.420185°	WV02
2019	2019-06-18T14:27:40	25.555307°	176.86177°	47.062794°	WV02
2018	2018-09-25T14:09:48	26.726582°	174.8811°	22.745913°	WV02
2017	2017-06-27T17:03:37	19.81273°	226.15402°	41.427032°	WV01
2015	2015-05-23T14:03:00	24.3746°	170.2943°	44.1565°	WV02
	2015-04-22T15:07:00	41.1564°	189.7850°	35.8205°	WV01

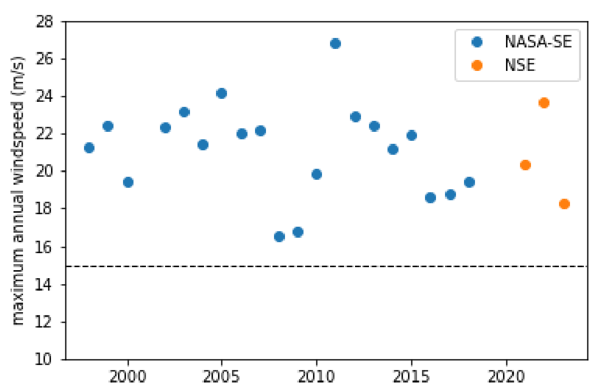

Fig. 9. Annual maximum wind speed as measured by weather stations NASA-SE (blue) and NSE (orange). The 15 m s^{-1} wind speed required for whaleback dune formation is marked with a dashed line.

collected by the PROMICE weather station `NSE` (66.47758°N, 42.49312°W) which monitored wind speed from 19 June 2021 through 01 Oct 2023. We use observations by the GC-NET automatic weather station `NASA-SE` located at (66.47789°N, 42.49438°W) which recorded data from 24 April 1998 through 31 December 2018 (Steffen and others, 2022). These data do yield a gap in measurements for 2019 and 2020, however, these missing data do not affect our interpretation because the extent of satellite imagery for 2019 and 2020 was also limited and we were unable to determine dune locations above 1,600 m elevations. Figure 9 shows annual maximum wind speeds from 1998 through 2023 as measured by `NASA-SE` and `NSE` as the maximum wind speed observed by either the stations upper or lower anemometer which were mounted with a vertical separation of one meter. These data show that wind speeds exceeded the 15 m s^{-1} threshold required for whaleback dune formation each year from 1998–2023, except for 2019–2020 where we do not have data. Whaleback dunes at the highest elevations on record were observed in 2023 with dunes forming sometime over the 2022–2023 winter (Fig. 7). Not only are 2021–2023 wind speeds similar to those recorded from 1998–2018, but the maximum wind speed in 2023 was lower than the maximum wind speed of 23.6 m s^{-1} in 2022 which was measured on 05 March 2022. Together these observations indicate that the expansion of whaleback dunes observed in 2023 cannot be explained by a change in wind conditions that had previously prevented whaleback dune formation.

APPENDIX B – LEFM MODEL EXTENDED DESCRIPTION

We follow the equation of van der Veen and Whillans (1989) to calculate the stress intensity factor associated with an tensile stress, $K_I^{(1)}$, which accounts for the presence of multiple closely spaced crevasses that shield neighboring crevasses from the tensile stress opening the crevasse. This equation assumes a constant crevasse spacing where a distance $2W$ separates neighboring crevasses. The function $D(S)$ in (3) describes the effect of shielding as a function of crevasse spacing following:

$$D(S) = \frac{1}{\sqrt{\pi}}\left[1 + \frac{1}{2}S + \frac{3}{8}S^2 + \frac{6}{16}S^3 + \frac{35}{128}S^4 + \frac{63}{256}S^5 + \frac{231}{1024}S^6\right] + 22.5S^7 - 63.5S^8 + 58.05S^9 - 17.58S^{10} \quad \text{(B1)}$$

where $S = \frac{W}{W+d}$ for crevasse depth d and crevasse spacing of $2W$. $D(S)$ approaches 1.12 as crevasse spacing increases such that (3) becomes equivalent to the expression for a single isolated crevasse.

The calculation of the stress intensity factor associated with the lithostatic or overburden pressure (4)

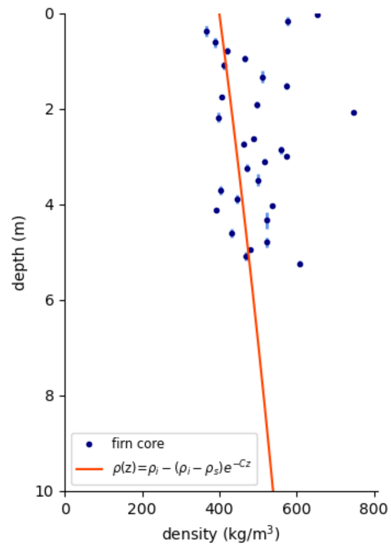

Fig. 10. Firn core measurements and depth-density relation fit (red) for $\rho_s = 400$ kg m^{-3} and $C = 0.0314$ m^{-1}. Navy dots mark the mid-point of the depth range for that given density and light blue lines mark the full depth range for a density measurement.

contains the functional expression $G(\gamma, \lambda)$ given by (Tada and others, 1973):

$$G(\gamma,\lambda) = \frac{3.52(1-\gamma)}{(1-\lambda)^{3/2}} - \frac{4.35-5.28\gamma}{(1-\lambda)^{1/2}} + \left[\frac{1.3-0.3\gamma^{3/2}}{(1-\gamma)^{1/2}} + 0.83 - 1.76\gamma\right] \times [1-(1-\gamma)\lambda] \tag{B2}$$

where $\gamma = z/d$ where z is depth below the surface, d is crevasse depth, $\lambda = d/H$, and H is ice thickness. The full expression for $K_I^{(2)}$ accounts for a lower density firn layer at the glacial surface which increases in density with depth.

Firn Density

To constrain the empirical snow density-depth formulation, $\rho(z)$, used to calculate the overburden pressure acting on the walls of crevasses in our LEFM model (4) we measured snow density in June 2023 from a 6 m firn core collected at our field site over the firn aquifer (Figs. 1b, 10). Snow density as a function of depth is calculated following (Cuffey and Paterson, 2010, p. 19):

$$\rho(z) = \rho_i - (\rho_i - \rho_s)e^{-Cz} \tag{B3}$$

where z is depth below the surface in meters, ρ_i is ice density taken to be 917 kg m^{-3}, ρ_s is surface snow density which is typically within the range of 300 to 400 kg m^{-3}. C is a site-specific empirical constant

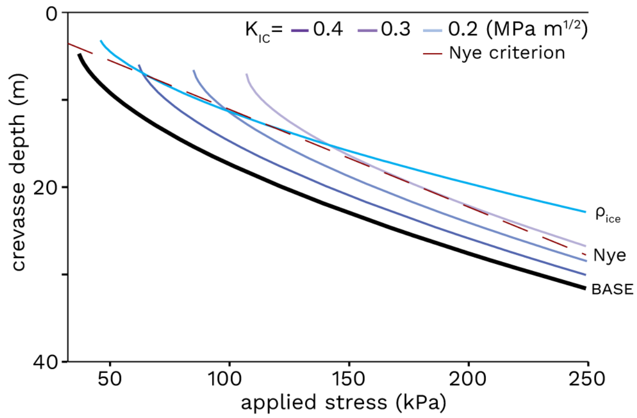

Fig. 11. Nye criterion crevasse depth comparison. Same as in Fig. 4a but with the Nye criterion in a red dashed line. Our base case is shown in bold (ρ_s=400 kg m^{-3}, K_{IC}=0.1 MPa, $2W$=50 m). Purple lines show model runs with variable K_{IC} and the cyan line shows a constant density solution where $\rho_s = \rho_i$.

that ranges from 0.0165 to 0.0314 m^{-1}. The snowpack exhibited high variability with depth; conditions ranged from sugar snow to ice and melt layers. We obtained values for ρ_s and C by least-squares fitting the data. We find a best fit of the snow density-depth formulation to our data occurs with a surface density ρ_s=400 kg m^{-3} and C=0.0314 m^{-1}, and use these values in (4).

APPENDIX C – NYE CRITERION

We compare our model results to the Nye criterion for crevasse depth (Nye, 1954; Weertman, 1977) which is shown in Figure 11. For closely-spaced, water-free crevasses the Nye criterion states that crevasse depth L is

$$L = \frac{T}{\rho_i g} \tag{C1}$$

where T is the tensile stress within the ice, ρ_i is the density of ice taken to be 917 kg m^{-3}, and g is acceleration due to gravity of 9.81 m s^{-2}.